

The December 2018 M_L 5.7 and January 2019 M_L 5.3 Earthquakes in South Sichuan Basin Induced by Shale Gas Hydraulic Fracturing

by Xinglin Lei, Zhiwei Wang, and Jinrong Su

ABSTRACT

An M_L 5.7 earthquake struck Xingwen County, Sichuan Province, China (28.239° N, 104.922° E) on 16 December 2018. More than two weeks later on 3 January 2019, an M_L 5.3 earthquake occurred 8 km to the west. These were the largest and most damaging events in the Changning shale gas block and resulted in extensive damage to nearby farmhouses and other structures. Although the official hypocentral depths for both events are large than 5 km, the centroid moment tensor solutions based on the generated cut-and-paste method were very shallow (3 and 1.8 km for M_L 5.7 and 5.3, respectively). In addition, both events were very close to hydraulic-fracturing (HF) zones of horizontal wells, in which HF was ongoing. A convening chain of evidence, including spatiotemporal correlation between earthquakes and HF zones, statistic parameters of seismicity, and estimated overpressure required to activate the unfavorably oriented source faults of the largest events, suggests that a series of earthquakes were induced by HF at a depth of \sim 2.5–3 km. In the Changning block, thus far, 11 $M_L \geq 4.0$ events (including 3 $M_L \geq 5.0$) were observed since the systematic HF operation began in 2014. The Omori-type aftershock productivity is very low as compared to normal tectonic seismicity. In addition, estimated overpressure ranged from \sim 0.3 to 5.8 MPa for $M_w > 3.5$ events. The poroelastic stress changes are less than 1 MPa out of the treatment zones. Hence, overpressure-driven reactivation of pre-existing faults (most of them are unmapped and unfavorably oriented for slip under the present tectonic stress field) is considered to be the cause of these abnormal moderate-size earthquakes.

Supplemental Content: Waveform fits for the 16 December 2018 M_L 5.7 and January 2019 M_L 5.3 events, photos of large-scale rock collapses and landslides caused by the M_L 5.7 event, and relocated catalogs for the entire region.

INTRODUCTION

In recent years, associated with the rapid development of shale gas and hydraulic fracturing (HF, also known as fracking),

fracking-induced earthquakes of moderate size (M_L 3–5) have attracted growing public and scientific attention (Atkinson *et al.*, 2016; Bao and Eaton, 2016; Lei *et al.*, 2017; Meng *et al.*, 2019). Microseismic events produced directly by HF, which typically have a magnitude of less than 0.5 (Chen *et al.*, 2018; Zadeh and Talebi, 2018), provide very useful signals for fracture monitoring and operation management. However, repeated small- (M_L 1–3) to moderate-magnitude (M_L 3–5) earthquakes can result in damage in areas that historically have not experienced large earthquakes. To ensure that shale gas fracking can be carried out effectively and safely, destructive earthquakes must either be avoided or be mitigated. Clarifying the mechanism and geomechanical conditions of induced earthquakes, and thus further predicting the maximum magnitude of a potential earthquake that might be induced at a given site, is thus a scientific challenge.

It is worth noting that most HF operations do not induce felt earthquakes. In central United States, HF is directly responsible for a small percentage of the felt induced earthquakes, and most induced earthquakes are a result of the injection of wastewater for disposal (Rubinstein and Mahani, 2015). However, recent studies have shown that earthquakes induced by HF are also pervasive in some regions of Ohio (Skoumal *et al.*, 2015) and Oklahoma (Skoumal *et al.*, 2018). In contrast, felt earthquakes induced during HF operations are more common in western Canada (Bao and Eaton, 2016). In the Sichuan basin of China, both long-term (continuing for a few years to several tens of years) injections for disposal of wastewater (Lei *et al.*, 2008, 2013) and short-term (continuing over several months) injections for shale gas HF (Lei *et al.*, 2017; Meng *et al.*, 2019) caused felt-induced seismicity resulting in sizable earthquakes up to M 5. Similar to other sites (Atkinson *et al.*, 2016), a high level of HF-induced seismicity and moderate-magnitude earthquakes were limited to some sites in the Sichuan basin. Among several shale gas blocks in the Sichuan basin, the Changning block demonstrated the highest level of induced seismicity (Fig. 1). Following a number of M_L 4–5 earthquakes in 2017, an M_L 5.7 earthquake occurred on 16 December 2018. This event was the most

damaging one so far, injuring 17 people, causing large-scale landslides and rock collapses (Figs. S3–S5, available in the supplemental content to this article), the collapse of nine houses, extensive damage to more than 390 houses, and a direct economic loss of \sim 50 million Chinese Yuan Renminbi (Sina Corp., 2019). Only 18 days later, another large event of M_L 5.3 occurred on 3 January 2019 in the southwest direction at a distance of 8 km.

This article focuses on (1) the analysis of the M_L 5.7 and 5.3 earthquakes (hereafter, mainshocks); (2) statistic features of seismicity since June 2018 in a small area, which covers both mainshocks; (3) inversion of the regional mean stress pattern within the Changning shale gas block from well-determined moment tensor solutions of all M_L 3.5+ earthquakes; and (4) estimation of the pore overpressure required to cause these events.

OVERVIEW OF HYDRAULIC FRACTURING AND SEISMICITY IN THE CHANGNING SHALE GAS BLOCK

The Changning shale gas block is located in the fold zone of the south boundary of Sichuan basin, China (Fig. 1). This block corresponds to a flat syncline (surrounded by narrow anticlines), and the target Silurian mudstone/shale formation has a burial depth of from less than 2 to more than 3 km. Vertical wells have been drilled for shale gas prospecting since 2008. Horizontal drilling began in 2011, and systematic HF in horizontal wells began in 2014 (Lei et al., 2017). In the Changning block, a typical well pad generally has four to eight wellbores with horizontal lengths of up to \sim 2500 m and an interval of 300–400 m between the lateral portions of two neighboring wells. A multistage zipper-fracturing technique was normally applied for treatment. On average, more than 1800 m³ of water is required for a single stage. The average wellhead pressure is \sim 60–70 MPa (Ren et al., 2015).

Coinciding with the start of systematic HF in horizontal wells, the observed earthquake rate increased dramatically in the Changning block. During the period from December 2014 to 20 February 2017, major HF activities were concentrated in the southwestern portion of the Changning block. In the mean time, more than 2400 $M_L \geq 1.0$ events were observed, including 8 $M_L \geq 4.0$ events and 1 M_L 5.0 (M_w 4.7) event that occurred on 17 February 2017, which resulted in 23 houses collapsing and 548 houses being heavily damaged (Lei et al., 2017). In 2018 and later, major HF activities were moved to the northeastern and south portions (Fig. 1) of the Changning block. Consistently, major seismic clusters were also migrated to the active HF sites (Figs. 1 and 2). The record of the maximum magnitude was soon renewed by the 16

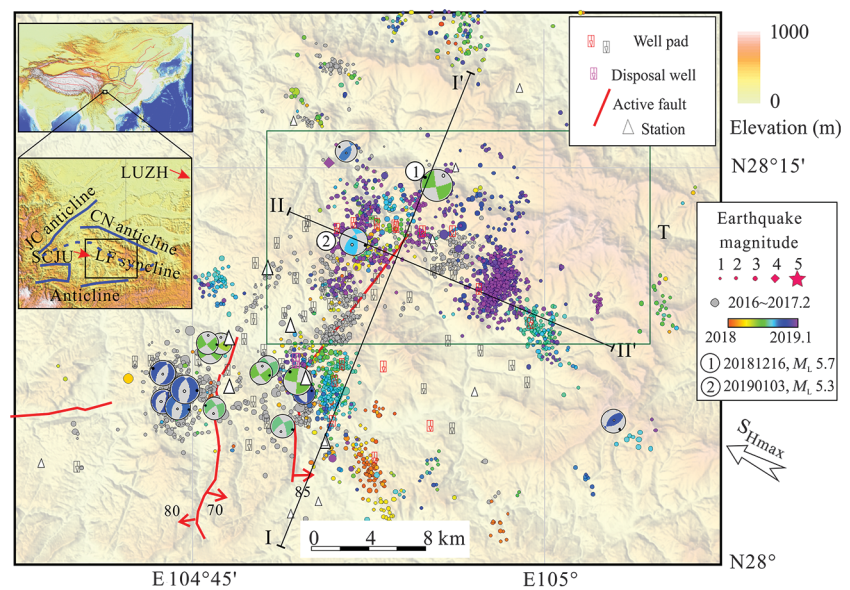


Figure 1. Map view of relocated hypocenters for two periods: (1) from 1 January 2016 through February 2017 (from Lei et al., 2017); and (2) from 1 January 2018 through January 2019. Focal mechanisms of $M_w > 3.5$ earthquakes since 2014 are shown with the lower-hemisphere projection of focal spheres. Well pads, in which hydraulic-fracturing (HF) activities were performed since 2018, are shown in red symbol. The pink color indicates the injection well for disposal of wastewater, whereas gray symbols show well pads in production or in drilling. Red arrows and numbers on the faults indicate the dip direction and dip angle of the fault. The large inward-pointing arrow shows the orientation of the maximum horizontal principal stress ($S_{H\max}$) obtained by this study. The inset maps show location and major structures in the Changning shale gas block and surroundings. Red arrows in the index map indicate crust movement at two Global Navigation Satellite System stations (LUZH and SCJU; China Earthquake Networks Center [CENC], 2018). T indicates the focused area (Fig. 2) of this study.

December 2018 M_L 5.7 and 3 January 2019 M_L 5.3 events. The M_L 5.7 event was abnormally destructive, with a maximum hazard level of VII. The VII area extends for more than 10 km along an east-southeast-extending valley (Sichuan Earthquake Administration [SEA], 2019; Fig. 2).

METHOD

Hypocenter Relocation

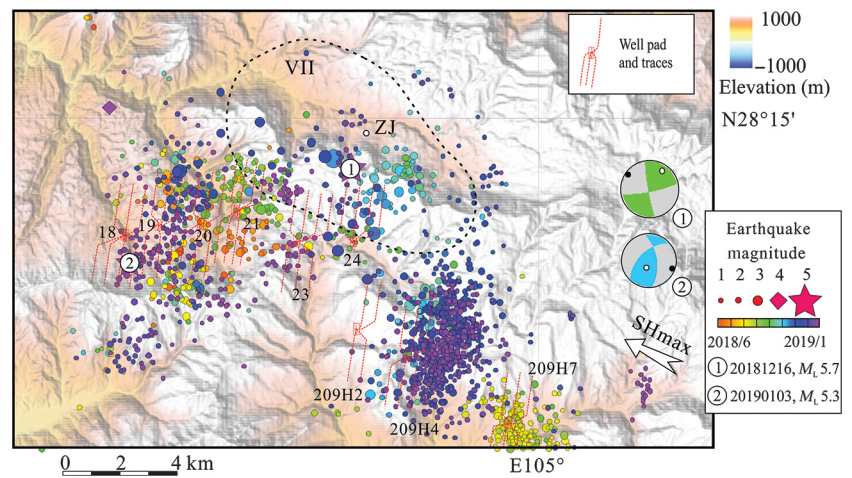
We used catalog phase data and the Hypocenter Double-Difference (HypoDD) program (Waldauser and Ellsworth, 2000) to relocate the earthquake hypocenters. The 1D velocity model used in a previous study (Lei et al., 2017) was used. In this study, we focused on two periods from January 2016 to February 2017 and from January 2018 to January 2019. The resulting hypocenter locations showed improvements but remained imprecise, with estimated horizontal errors from 200 to 600 m and vertical errors from 200 to 800 m. For the period from January 2016 to February 2017, the results from Lei et al. (2017) were referenced. During this period, data from six portable stations were available, the hypocenters in the central area, which was covered by the portable stations, were determined with errors less than a few hundred meters.

Moment Tensor Inversion

The moment tensor was estimated using the generalized cut-and-paste (gCAP) method, which is advanced using the full waveforms of body and surface waves recorded by broadband seismometers (Zhu and Ben-Zion, 2013). In a previous study, the moment tensors of 13 earthquakes of $M_w > 3.5$ that occurred from 2014 to February 2017 were determined with good quality (Lei *et al.*, 2017). We applied the same approach and the same velocity model to later earthquakes. The original seismograms were typically filtered with corner frequencies (0.02, 0.15) or (0.02, 0.1). Unit weight was applied to all phases. Full moment tensors were estimated by a grid search with respect to the moment magnitude (step of 0.01) and the strike, dip, and rake angles (step of 5°) of the faults and slip orientations. The obtained full moment tensor is decomposed into double-couple (DC), isotropic (ISO), and compensated linear vector dipole (CLVD) components (Zhu and Ben-Zion, 2013). Beside the preferred velocity model, we also examined results obtained using some reference models and found that uncertainty of centroid depth due to velocity error is less than 200–400 m for most events.

Stress Inversion and Estimation of Fluid Overpressure

The crustal stress states can be partly estimated from the analysis of seismic data by stress inversion approach, in which the



▲ Figure 2. Zoomed map view showing active (during June 2018 through January 2019) HF pads and seismicity in the focused area of this study ("T" in Fig. 1). Relocated hypocenters for the period from 1 June 2018 through January 2019. Focal mechanisms of the 16 December 2018 M_L 5.7 and 3 January 2019 M_L 5.3 earthquakes are shown with the lower-hemisphere projection of focal spheres. VII indicates the area of hazard level VII of the December M_L 5.7 earthquake. The arrow and $S_{H\max}$ shows the orientation of the maximum horizontal principal stress obtained by this study.

Because fault slip cannot constrain the ISO part of the stress tensor, $\sigma_{33} = -(\sigma_{11} + \sigma_{22})$ is assumed. The matrix \mathbf{G} is derived from the fault-normal vector and given by (Hardebeck and Michael, 2006)

$$\mathbf{G} = \begin{pmatrix} n_{i1} - n_{i1}^3 + n_{i1}n_{i3}^2 & n_{i2} - 2n_{i1}^2n_{i2} & n_{i3} - 2n_{i1}^2n_{i3} & n_{i1}n_{i3}^2 - n_{i1}n_{i2}^2 & -2n_{i1}n_{i2}n_{i3} \\ n_{i2}n_{i3}^2 - n_{i2}n_{i1}^2 & n_{i1} - 2n_{i2}^2n_{i1} & -2n_{i1}n_{i2}n_{i3} & n_{i2} - n_{i2}^3 + n_{i2}n_{i3}^2 & n_{i3} - 2n_{i2}^2n_{i3} \\ n_{i3}^3 - n_{i3}n_{i1}^2 - n_{i3} & -2n_{i1}n_{i2}n_{i3} & n_{i1} - 2n_{i3}^2n_{i1} & n_{i3}^3 - n_{i3}n_{i2}^2 - n_{i3} & n_{i2} - 2n_{i3}^2n_{i2} \end{pmatrix}, \quad (3)$$

average stress patterns of prepartitioned blocks are determined from the fault-slip data of earthquakes with the least-squares method (e.g., Gephart and Forsyth, 1984; Michael, 1987; Hardebeck and Michael, 2006). By assuming that seismic slip occurs in the direction of the resolved shear traction acting on pre-existing faults, a stress pattern can be determined from a variety of focal mechanisms (Gephart and Forsyth, 1984). The slip vector \mathbf{d} on a fault plane is given by

$$\mathbf{d} = \mathbf{G}\mathbf{m}, \quad (1)$$

in which \mathbf{m} is a vector of stress-tensor component:

$$\mathbf{m} = \begin{pmatrix} \sigma_{11} \\ \sigma_{12} \\ \sigma_{13} \\ \sigma_{22} \\ \sigma_{23} \end{pmatrix}. \quad (2)$$

in which i indicates the i th fault. To estimate \mathbf{m} , slip data on at least two faults of different orientations are required. For slip data on multiple faults, the least-squares inversion solution is given by

$$\mathbf{m} = \mathbf{G}^T \mathbf{d} (\mathbf{G}^T \mathbf{G})^{-1}. \quad (4)$$

This standard method can be expanded to invert for a regional, possibly varying stress field. Mean stress in spatial and temporal boxes is solved by the damped inversion method, which minimizes the weighted sum of the data misfit and the model length (Hardebeck and Michael, 2006). Because the study area is small, we used the least-squares method to estimate the mean stress pattern. For examining the uncertainty of the inversion results, the standard errors were estimated using the Monte Carlo approach. We made 5000 runs by

randomly choosing one of the nodal planes to be considered as the source faults.

By further assuming that (1) seismic slip occurs following Coulomb failure criterion with the standard friction coefficient of 0.6, (2) the vertical stress is the weight of the overburden, and (3) optimally oriented faults are critically stressed to the prevailing regional stress pattern with hydrostatic fluid pressure, it is possible to estimate the Coulomb failure stress (CFS) and the pore overpressure at the source region of earthquakes with well-determined mechanism solutions (Terakawa *et al.*, 2012). Assumption (1) is partly supported by experiment data for several kinds of rocks from Sichuan basin (Lei *et al.*, 2014). As mentioned previously, the study area is located in the fold zone of the southern Sichuan basin, in which background seismicity is low but not zero. Thus, assumption (3) is also reasonable.

Coulomb Failure Stress

The CFS transferred from the fault slip of the M_L 5.7 event was calculated based on the Okada dislocation model (Okada, 1992). The elastic medium was assumed to be homogeneous and ISO with a shear modulus of 32 GPa and Poisson's ratio of 0.25. The coulomb stress is calculated according to the following equation:

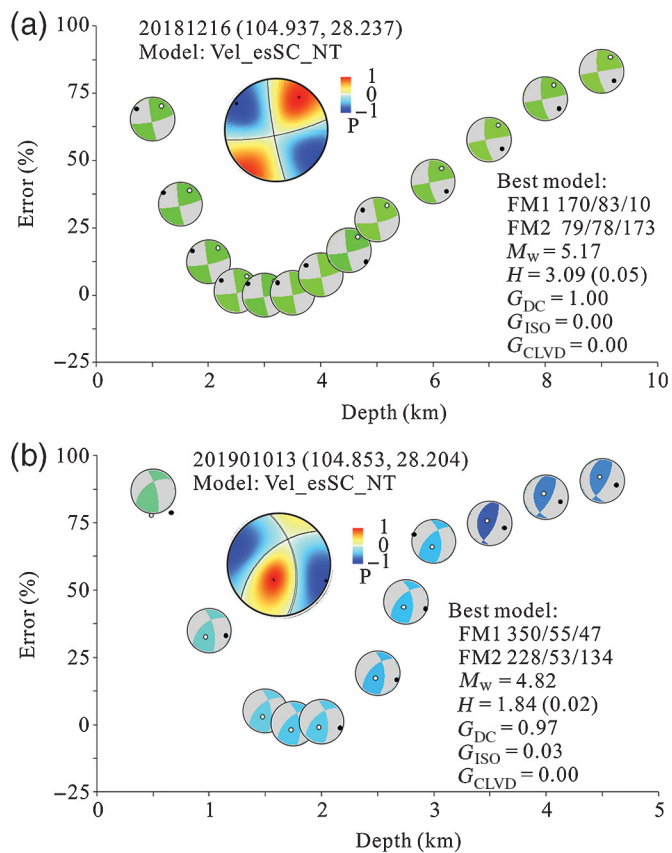
$$\Delta\text{CFS} = \Delta\tau + \mu(\Delta\sigma + \Delta P), \quad (5)$$

in which μ is the frictional coefficient ($= 0.6$), $\Delta\tau$ and $\Delta\sigma$ are changes in the shear and normal stresses, respectively, on given receiver faults for the given strike, dip, and rake. Moreover, ΔP is the unrelaxed pore pressure change, which is defined as $\Delta P = B\Delta\sigma_m$, in which σ_m is the mean stress, and B is the Boit's coefficient.

MOMENT TENSOR AND FOCAL DEPTH OF THE M_L 5.7 AND M_L 5.3 EARTHQUAKES

The M_L 5.7 and 5.3 earthquakes have been recorded by many broadband seismic stations from the regional seismic networks. For the M_L 5.7 earthquake, we selected seismograms from 33 stations within a distance of 300 km to invert the full moment tensor using the gCAP method. The best-fit centroid moment depth is 3.09 km (Fig. 3a). The estimated moment magnitude was M_w 5.2, and two nodal planes were estimated as (strike, dip, rake) = (170, 83, 10) and (79, 78, 173), thereby indicating that the event was a typical strike-slip-dominated event. This event revealed pure DC mechanisms, that is, the squared ratios of the scalar potency of the non-DC components to the total scalar potency, of less than 0.5%.

For the M_L 5.3 earthquake, waveforms from 24 stations were used. The best-fit centroid moment depth is 1.84 km (Fig. 3b), shallower than the HF zone. The estimated moment magnitude was M_w 4.8, and two nodal planes were estimated as (strike, dip, rake) = (352, 55, 51) and (227, 50, 132), thereby indicating that both strike-slip and reverse components are almost equally important. This also showed a pure DC



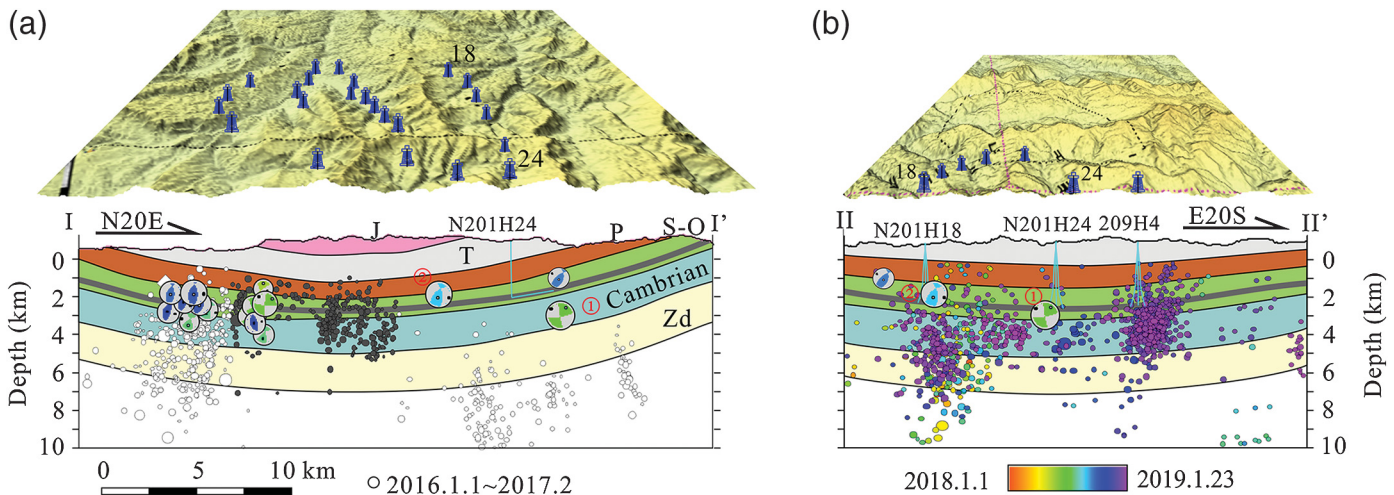
▲ **Figure 3.** Comparison of misfit error of moment tensor inversions by the generalized cut-and-paste method with respect to the assumed focal depth for the (a) 16 December 2018 M_L 5.7 and (b) 3 January 2019 M_L 5.3 earthquakes. The color scale in the large focal mechanisms indicates the P -wave radiation pattern. The mechanism solutions and radiation pattern are shown by lower-hemisphere projection of the focal spheres. Strike/dip/rake of the nodal planes (FM1 and FM2), resolved moment magnitude (M_w), focal depth (H), double-couple (G_{DC}), isotropic (G_{ISO}), and compensated linear vector dipole (G_{CLVD}) components are indicated.

mechanism with an estimated ISO component of 3%, falling into the range of error.

Azimuth distribution of stations used and waveform fitting plots (Figs. S1 and S2) show that the moment tensor solutions are well determined for both M_L 5.7 and 5.3 earthquakes.

CORRELATION BETWEEN EARTHQUAKES AND HF ZONES

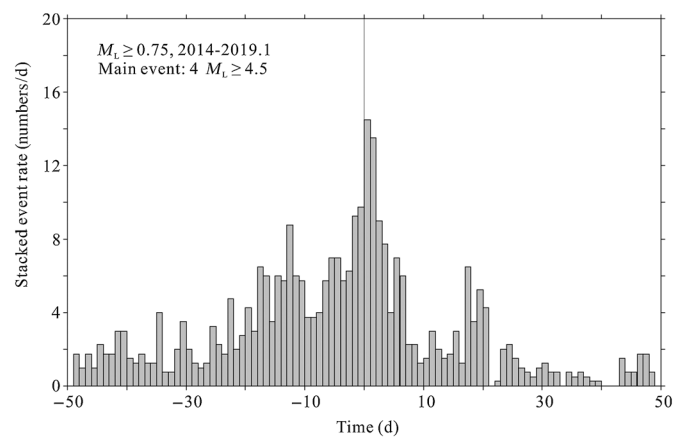
Figure 4 shows a simplified geological section overlaid with some relocated hypocenters and focal mechanisms of $M_w > 3.5$ earthquakes. All of the $M_w > 3.5$ earthquakes had a centroid depth between 1.9 and 4.0 km. For shallow earthquakes, surface waves impose a robust constraint on focal depth estimations (Lei *et al.*, 2017). The top 3D-shaded images show



▲ Figure 4. Simplified geological sections (defined in Fig. 1) overlapped with relocated hypocenters for earthquakes observed (a) from 1 January 2016 to 23 February 2017 (Lei *et al.*, 2017) and (b) from 1 June 2018 to 23 January 2019. Dark gray circles indicated the well-determined hypocenters covered by portable stations. Focal mechanisms of $M_w > 3.5$ earthquakes are shown with the lower-hemisphere projection of focal spheres. The top 3D-shaded image shows the landscape and well pads in which HF was performed or is ongoing.

the landscape and part of the well pads. Hypocenters for the period from 1 January 2016 to 23 February 2017 are plotted. For this period, hypocenters were well determined using the double-differential method (see the *Method* section for details) and catalog data from permanent stations as well as six portable seismic stations (Lei *et al.*, 2017). The depth distributions of the relocated hypocenters were centered at the target zone of the shale formation, which contains the producing interval that was being hydrofracked. For other periods, only data of the permanent stations were open to the public, and the relocated hypocenters were scattered in a depth range of from 2 km to more than 10 km, probably due to poor precision, especially in regard to depth. A number of additional stations were installed in 2018, by which precision of hypocenter locations was improved. As seen from Figure 4b, earthquakes since December 2018 were concentrated in depths of from 2 to 6 km. Thus, the M_L 5.7 mainshock and its preshocks and aftershocks were spatially correlated with the front zone of the northward horizontal wells of an active shale gas pad (N201-H24; Fig. 2). Based on a field survey, HF in this pad began in October 2018 and completed on 13 January 2019. After the M_L 5.7 earthquake occurred, ongoing HF operations in Changning block had been paused for some days. In map view, the hypocenter of the M_L 5.3 earthquake was located within treatment zone of well pad N201-H18. HF at the southward wells of N201-H18 began in November 2018 and was ongoing during the M_L 5.3 earthquake occurrence (Fig. 2). As a result, the spatiotemporal correlation between HF wells and seismic burst raise the possibility that the main earthquakes and other events observed here were HF-induced.

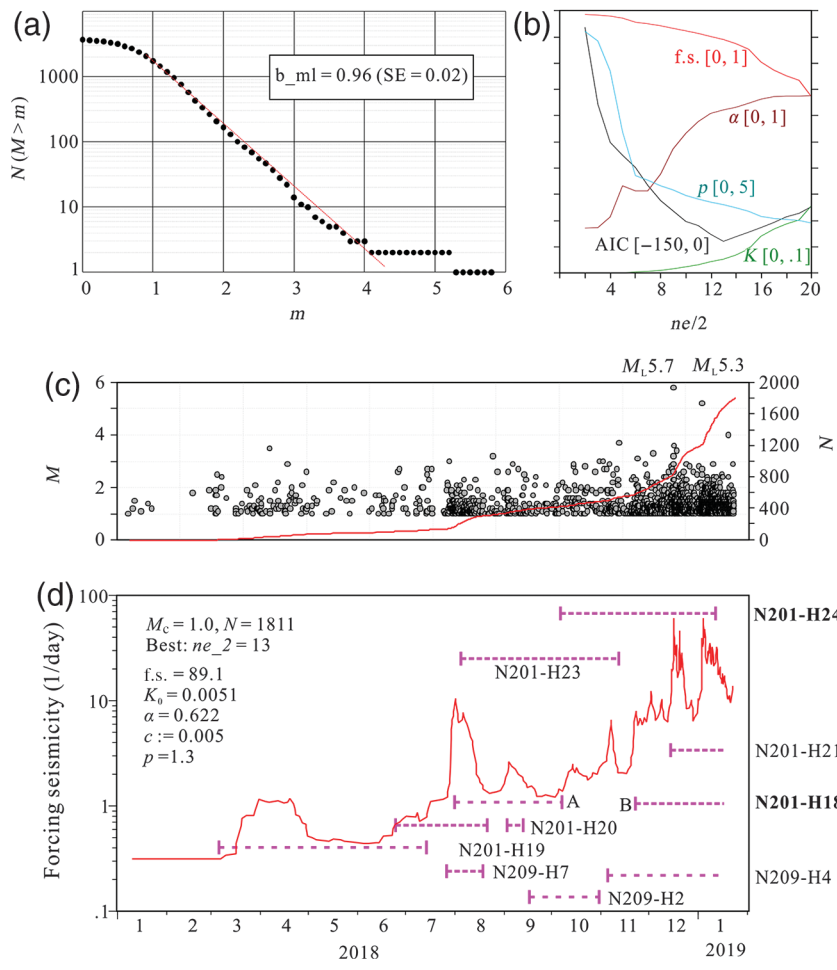
For tectonic seismicity, large events were followed by a large number of aftershocks but foreshocks are normally rare. However, injection-induced seismicity generally demonstrates



▲ Figure 5. Stacked event rate of apparent foreshocks and aftershocks of four $M_L \geq 4.5$ earthquakes.

very low aftershock productivity. We examine the statistical features of the observed seismicity. For seismicity in the Changning block, stacked event rates of apparent foreshocks and aftershocks of $M_L \geq 4.5$ earthquakes demonstrate increasing event rate of foreshocks in the past 30 days before the mainshocks, whereas aftershock rate dropped quickly within several days (Fig. 5).

Because induced seismicity in the Changning block before June 2017 was reported in a previous paper (Lei *et al.*, 2017), we herein focus on injection activity and seismicity in the time span from 1 June to 31 December 2018 and in an area centered at the N201-H24 well pad (Fig. 2). Figure 6a and 6c shows the magnitude-time plot and the magnitude-frequency distribution. The lower cutoff magnitude for completeness is 1.0. The maximum-likelihood b -value for our dataset is 0.96. The variation of the b -value was reported for different cases of



▲ Figure 6. Earthquakes and major HF periods in the focused area of this study (Fig. 2). (a) Magnitude–frequency distribution, b -value, and its standard error (SE) estimated by the maximum-likelihood method. (b) Epidemic-type aftershock sequence (ETAS) parameter K , α , p , and Akaike information criterion (AIC), together with the total fraction of forced seismicity (f.s.). The minimum AIC is obtained for $ne/2 = 13$ (in which ne is the length of the smoothing window for the event number). (c) Magnitude–time plot and accumulative event number with respect to time. (d) F.s. from ETAS model of $M \geq 1.0$ earthquakes, and major HF time windows at well pads in the focused area.

HF-induced seismicity, typically from 0.8 to 1.20 for out-of-zone seismicity, which reaches to 2.0 for near-zone microseismicity (Chen *et al.*, 2018; Kozlowska *et al.*, 2018). Thus, as expected, the b -value of the seismicity in the study area falls in the typical range of out-of-zone seismicity.

We further applied our seismic dataset to the epidemic-type aftershock sequence (ETAS) model, which is useful for statistically separating total seismicity into external forced activity (here, induced by HF) and Omori-type aftershocks. When used with a time-varying forcing rate, the ETAS model results show that the forced seismicity (f.s.) accounts for 89% of seismicity, whereas the Omori-type aftershock productivity is very low (Fig. 6d). These features, similar to earlier seismicity in the same shale gas block (Lei *et al.*, 2017), indicated that the seismicity here was driven by fluid pressure. Next, we estimated

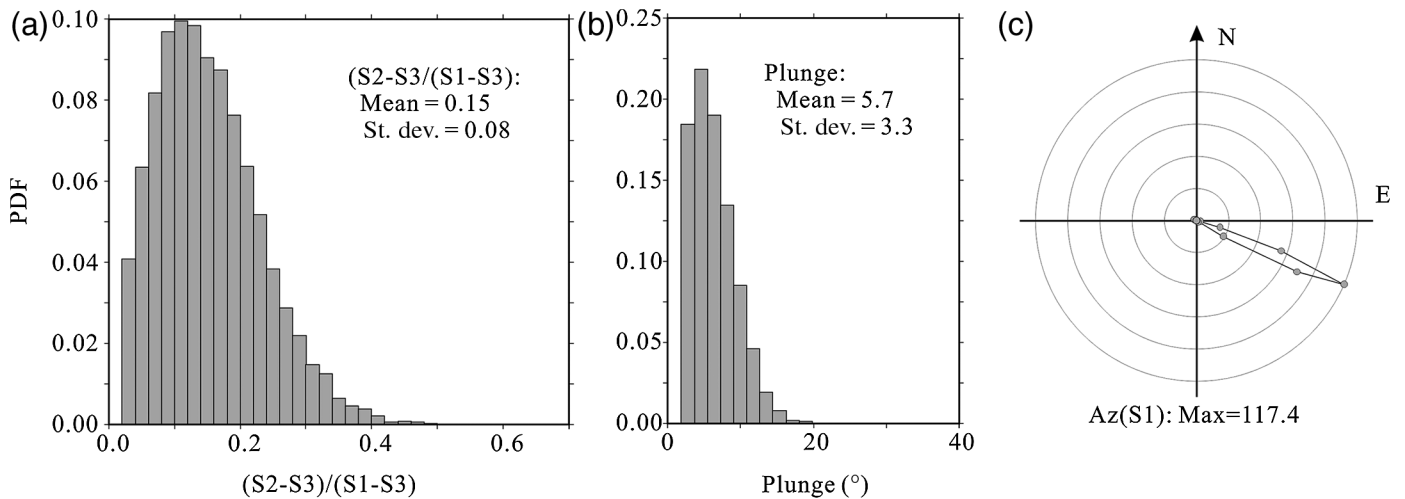
the magnitude of overpressure required to activate faults in the Changning shale gas block.

ESTIMATION OF OVERPRESSURE FOR $M_w > 3.5$ EVENTS

Together with earlier published data in Lei *et al.* (2017), there are 18 reliable mechanism solutions for earthquakes of $M_w > 3.5$. The directions of three principal stress axes and stress ratio ($R = (S_2 - S_3)/(S_1 - S_3)$) and their standard errors can be estimated using the stress inversion method described in the Method section. As shown in Figure 7, the direction of the maximum horizontal principal stress axis was well resolved and is almost horizontal (plunge: 5.7 ± 3.3) and has a azimuth of 117° , which is in very good agreement with that indicated by borehole breakout data (Lei *et al.*, 2017), results of stress measurement of the Longmaxi formation (Wang *et al.*, 2016), and crust movement data observed at two nearby Global Navigation Satellite System stations (Fig. 1). The obtained stress ratio was $R = 0.15$ with a standard error of 0.08, which means that the 95% confidence interval of R is $[0.07, 0.23]$. Such stress pattern is consistent with the maximum and minimum horizontal *in situ* stresses, which show a deviated stress of ~ 22 MPa within the shale formation (Wang *et al.*, 2016).

We further estimate the CFS required causing these $M_w > 3.5$ earthquakes. A mean value of $R = 0.15$ was used. To examine the effect of the uncertainty of R , the results for an extreme case of $R = 0.023$ were also considered. Under such a low R -value, the medium (horizontal) and minimum principal stresses have approximately equal magnitude, and thus the results can be considered as a lower bound. For most events, we do not know which nodal plane provided the real source fault; we thus cal-

culated CFS for both nodal planes and simply chose the nodal plane based on which nodal plane had the smaller CFS. Both the poroelastic effect and overpressure contribute to changing the CFS of a given fault. Detailed analysis relies on hydra-thermo-mechanic-coupled simulation. Here, the overpressures were simply calculated by ignoring the CFS from solid deformation. Figure 8 shows the focal mechanisms of $M_w > 3.5$ earthquakes projected in the normalized Mohr diagram. Table 1 lists results for all $M_w > 3.5$ earthquakes. As shown in Figure 8 and Table 1, an CFS increment of from 0.2 to 3.5 MPa or an overpressure from 0.3 to 5.8 MPa was necessary to cause these $M_w > 3.5$ earthquakes. Based on the numerical simulation results of Lei *et al.* (2017), the region of $CFS \geq 1$ MPa from the poroelastic effect is limited within the HF zone and very narrow bands surrounding this zone.



▲ Figure 7. Estimated stress ratio of the (a) principal stresses ($S_1 - S_3$) and the orientation ([b] plunge and azimuth [c] angles) of the maximum principal stress axis. PDF, probability density function.

Thus, the poroelastic effect could be a significant contributor only for events located close to the HF zones. At the same time, the poroelastic effect also responds to earthquakes on critically stressed faults (having a favorable orientation). For critically stressed faults, the change in CFS (Δ CFS) on the order of 0.01 MPa can trigger significant earthquakes (Cochran *et al.*, 2004). Direct overpressure must respond more to most $M_w > 3.5$ earthquakes, the hypocenters of which were located far from the HF zone at a distance of more than ~ 100 m. Because the injection pressure at the Changning site was ~ 70 MPa on average, which is sufficient to raise the fluid pressure of a nearby fault if the fault penetrated the HF zone or connected with the HF zone through permeable fluid pathways.

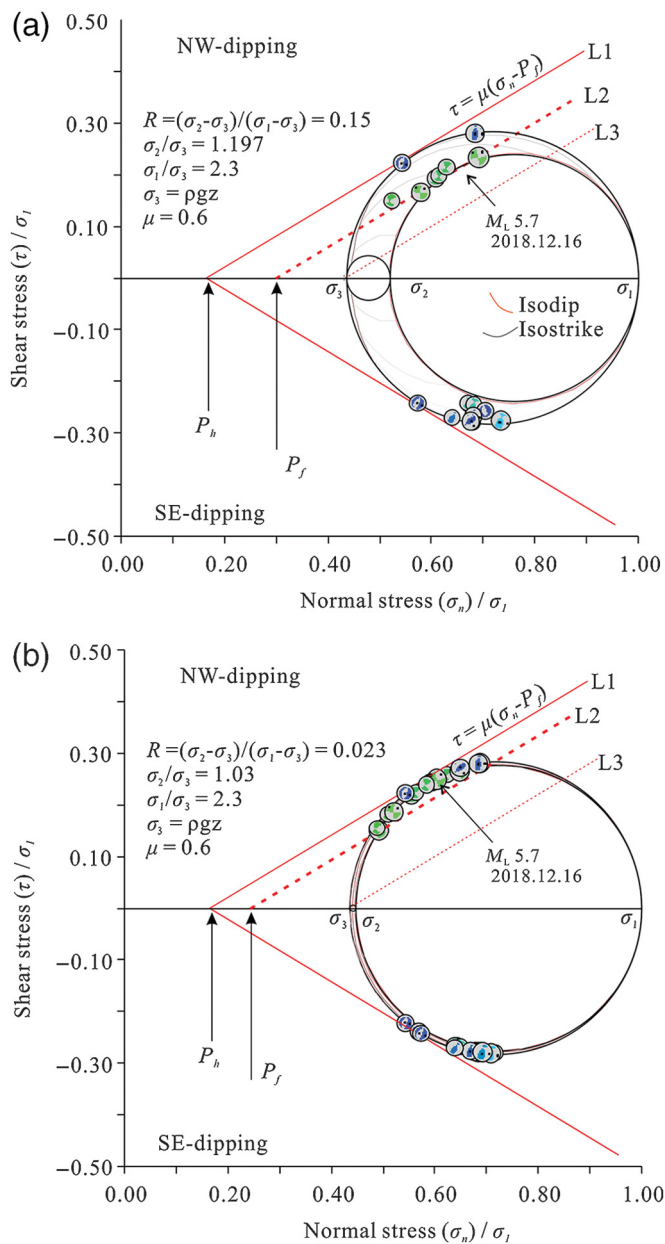
The $M_L 5.7$ was followed by some aftershocks of $M_L \leq 3.2$. The Δ CFS transferred from the fault slip of the $M_L 5.7$ event was calculated based on the Okada dislocation model (see the Method section for detail). Based on the aftershock distribution and local geology structure, the nodal plane of (strike, dip, rake) = (170, 83, 12) was considered to be the source fault. The fault area was estimated according to the empirical relationship between the moment magnitude and the rupture dimension: $M_w = \log_{10} A - 2.0$ (in which A is rupture area in m^2 ; Leonard, 2010). The slip was calculated from $M_0 = GuA$, in which M_0 is the moment, G (30 GPa) is the shear modulus of the elastic medium, and u is the displacement. Figure 9 shows the distribution of Δ CFS, which was calculated for receiver faults of an orientation same to the $M_L 5.7$ main event and a depth of 4 km, overlapped with three days fore-aftershocks and aftershocks. Indeed, some aftershocks (including two $M \sim 3$ events) fall in regions of positive Δ CFS. However, major aftershock zones, especially the southeast one, were located out of the central region of greater Δ CFS but close to active HF zones. Many aftershocks were located in the east side of N209-H4 well pad, in which ongoing HF was paused after the $M_L 5.7$ earthquake. As aforementioned, all HF activities were paused for

several days. This is evidence indicating overpressure raised by ongoing HF activities make the region more prone to seismic triggering. Similarly, dynamic triggering by the passing surface waves from distant earthquakes was observed in another shale gas site in the Sichuan basin (Han *et al.*, 2017).

For examining whether the $M_L 5.3$ event was triggered by the $M_L 5.7$ event, we calculated Δ CFS for faults having (strike, dip, rake) and a depth that are the same as for the $M_L 5.3$ earthquake. As seen from Figure 10, the resulting Δ CFS values at the hypocenter of the $M_L 5.3$ earthquake are negative. We also calculated Δ CFS from another fault plane of (strike, dip, rake) = (79, 78, 173) of the $M_L 5.7$ event. This time, the estimated Δ CFS values at the hypocenter of the $M_L 5.3$ earthquake are positive but the values are small, and are much lower than the value of 3 MPa, required as the cause of the $M_L 5.3$ earthquake. Therefore, the $M_L 5.3$ event was not triggered by the $M_L 5.7$ earthquake. It was likely induced by ongoing HF in N201-H18 pad.

DISCUSSION AND CONCLUSIONS

In summary, the present study shows a convening chain of evidence, suggesting that the $M_L 5.7$ and 5.3 earthquakes were induced by nearby HF activities. First, both the $M_L 5.7$ and 5.3 earthquakes were located very close to HF zones of horizontal wells, in which HF was ongoing when the earthquakes occurred. Second, results of ETAS models of seismicity before and after the mainshocks indicated that the f.s. was dominated, whereas the Omori-type aftershock productivity is very low. These features, similar to earlier seismicity in the same shale gas block (Lei, *et al.*, 2017), indicated that the seismicity here was driven by external forcing (fluid pressure). Third, the estimated overpressure, required to activate the unfavorable source faults of $M_w > 3.5$ events, ranged from 0.2 to 5.8 MPa. Because the poroelastic stress changes are less than 1 MPa out of the



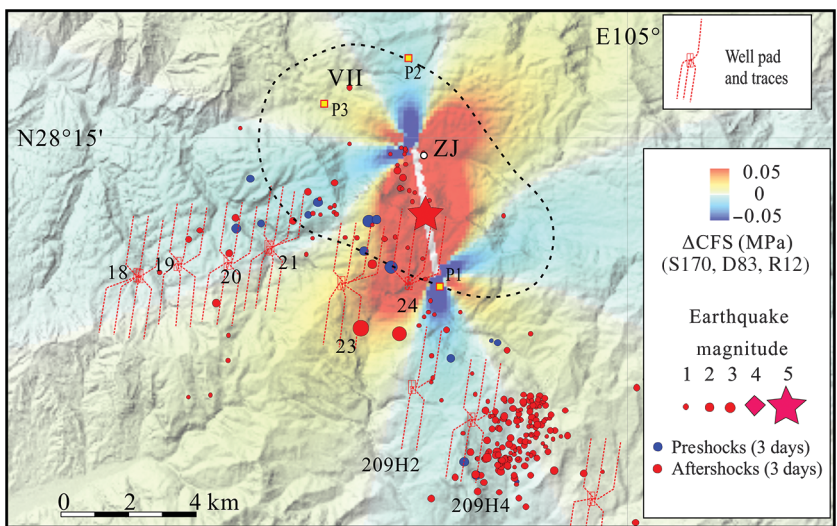
▲ Figure 8. Focal mechanisms of $M_w > 3.5$ earthquakes are shown in the 3D Mohr diagram (normalized by the maximum principal stress) of (a) $R = 0.15$ and (b) $R = 0.023$ by lower-hemisphere projection of the focal spheres. Lines L1, L2, and L3 indicate the fault strengths under hydrostatic, intermediate, and lithostatic fluid pressures, respectively.

treatment zones, we suggest that overpressure-driven reactivation of pre-existing faults (most of them are unmapped and unfavorably oriented for slip under the present tectonic stress field) is considered to be the cause of these abnormal moderate-size earthquakes. Thus far, injection-induced earthquakes with a magnitude greater than 5.5 have been documented at sites of wastewater disposal (Skoumal *et al.*, 2018) and an enhanced geothermal system (Kim *et al.*, 2018). The $M_L 5.7$ Xingwen earthquake is, at present, the largest HF-induced earthquake.

In the Sichuan basin, both short-term HF and long-term disposal of wastewater induced significant earthquakes in the past. The injected fluids need not migrate from the injection well to a fault for fault reactivation. The fault is reactivated by the increase in fluid pressure, which can be transmitted across greater distances than fluids themselves due to the low compressibility of the fluids. Injection-induced seismicity demonstrated strong dependence of sites (Rubinstein and Mahani, 2015; Bao and Eaton, 2016). At some sites, such as in Oklahoma, it was suggested that poroelastic stresses are likely responsible for HF-induced seismicity (Skoumal *et al.*, 2018). In the Duvernay play, geological factors play a prominent role in seismic productivity, whereas a linear correlation between injected volume and the induced earthquake rate has been found near Fox Creek (Schultz *et al.*, 2018). Such a statistical correlation probably represents the mean behavior of many wells.

Under certain conditions, earthquake ruptures can be confined to a pressurized region. In contrast, under other conditions, earthquakes are able to propagate as sustained ruptures outside of the zone that experienced a pressure perturbation (Norbeck and Horne, 2018). Governing factors may include, but are not limited to, the criticality of the regional stress level, the brittleness of the reservoir and overlying and underlying layers, the immaturity and geometric complexity of pre-existing faults, the fault orientation relative to the principal stresses, the fluid pathways, dynamic evolution of the fault zone properties, and *in situ* overpressure (Ellsworth, 2013; Eaton and Schultz, 2018; Kozłowska *et al.*, 2018). At the same time, the duration of injection, the injection pressure, and the volume of injected fluid will also strongly influence whether earthquakes will be induced and how large they will be. For individual sites, the site-dependent features may lead to various seismic responses to HF. Therefore, it is very important to determine the relative influence of these effects on inducing earthquakes at individual sites.

In the Sichuan basin, systematic and large-scale HF activities were carried out in four sites: Jiaoshiba, Changning, Weiyuan, and Weixi (west Weiyuan). The Weiyuan shale site is located in the central uplift of the Sichuan basin and also shows a high level of injection-induced seismicity. However, despite the fact that HF treatments in the same Longmaxi shale formation were performed with higher fluid pressure than used at the Changning site, the largest earthquake observed so far was an $M_L \sim 3.6$ event. The west Weiyuan site is located in the southeast slope of the Weixi anticline. Since 2016, six earthquakes of $M_L 4\text{--}4.9$ were observed. The most recent one, an $M_L 4.9$ event on 25 February 2019, killed two persons. Different responses in Weiyuan, Weixi, and Changning sites were interpreted by the differences in scale and density of pre-existing faults. When compared with the southern fold zone, sediment deformation in the central uplift of the Sichuan basin is relatively weak and show fewer faults in the sedimentary layers (Lei *et al.*, 2017). The Jiaoshiba site is located in the southeastern fold zone and thus shows higher density of faults, similar with the Changning and Weixi sites.



▲ Figure 9. Map view showing active (during June 2018 through January 2019) HF pads and three days preshocks and aftershocks of the 16 December 2018 M_L 5.7 earthquake. The shaded background image shows change of Coulomb failure stress (ΔCFS) from the M_L 5.7 earthquake to receiver faults of (strike, dip, rake) = (170, 83, 12) and depth of 2 km. P1 ~ 3 indicates sites of large-scale collapses and landslides (see ② Figs. S3–S5, available in the supplemental content to this article). ZJ indicates the location of Zhoujia village, which suffered the most extensive damages. Numbers 18–24 indicate well pad in N201 block, while 209H2 and 209H4 indicate well pads in N209 block.

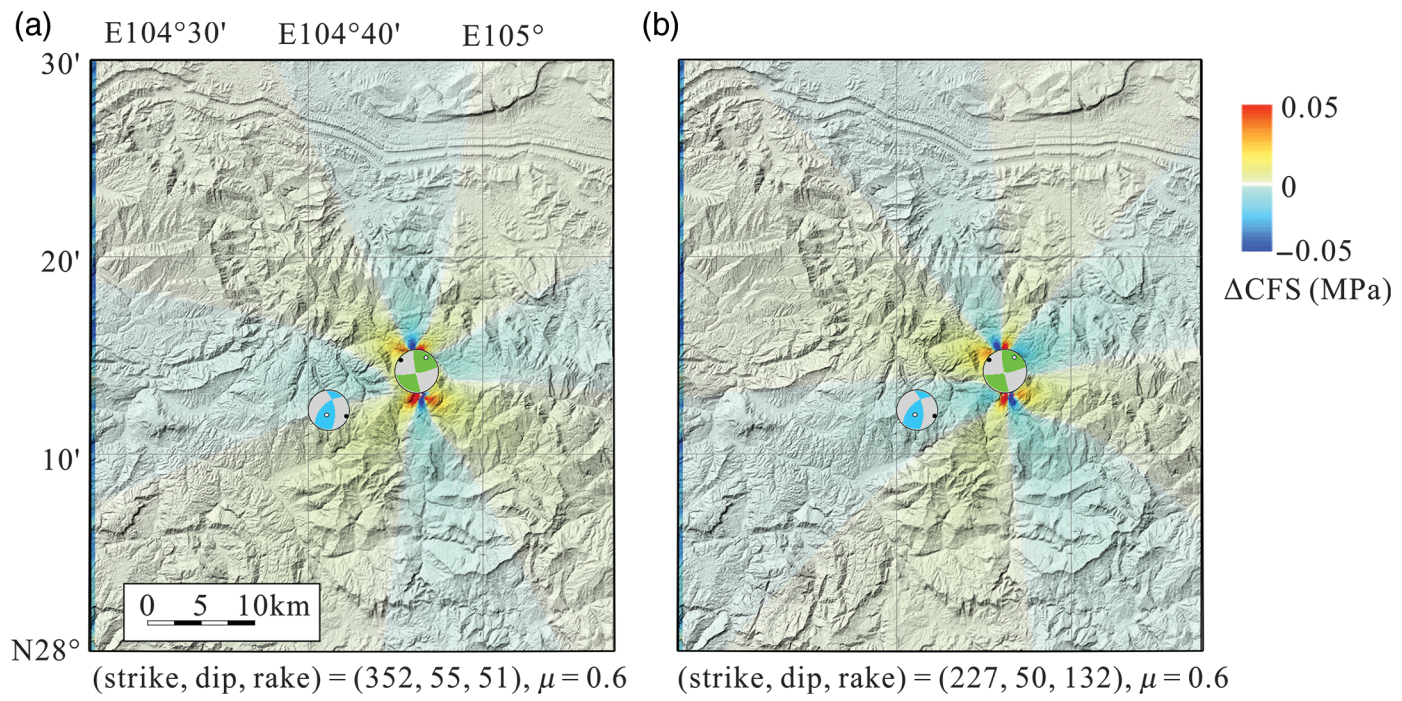
Interestingly, the Jiaoshiba shows the lowest level of induced seismicity. In the Jiaoshiba site, difference between the maximum and minimum horizontal *in situ* stress is small (3–7 MPa), significantly smaller than that in the Changning site (~22 MPa; Wang *et al.*, 2016). In addition, injection pressure for HF in the Jiaoshiba site was averagely 10 MPa lower than the Changning site. Thus, the lower seismicity in the Jiaoshiba site could be explained by the stress pattern, under which stress from HF was insufficient to activate unfavorable faults. It is an interesting issue for further studies.

At the Changning site, direct pore-pressure effects are thought to be a necessary condition, at least for the largest out-of-zone events. Their source faults were unfavorably orientated (due to stress rotation after their formation; Lei *et al.*, 2017) and thus required an additional load of CFS in order from ~1 MPa to more than 10 MPa, which is greater than that the poroelastic effect could produce. Indeed, we cannot rule out poroelastic stresses as a contributing factor, especially for events along favorably oriented faults of small scales or critically stressed faults due to local stress concentration.

Table 1
Pore Overpressure and Increment of Change of Coulomb Failure Stress (ΔCFS) at the Source Point of $M_w > 3.5$ Earthquakes Derived from Stress Pattern and Focal Mechanism Solutions

Number	Date (yyyy/mm/dd)	M_L	M_w	H (km)	Pf^1 (ΔCFS) (MPa)	Pf^2 (ΔCFS) (MPa)	Fault 1			Fault 2		
							Strike (°)	Dip (°)	Rake (°)	Strike (°)	Dip (°)	Rake (°)
1	2015/04/11	3.9	3.54	3.3	5.0 (3.0)	11.7 (7.0)	237	67	150	339	63	26
2	2015/04/24	4.2	4.05	3.0	2.7 (1.6)	12.8 (7.7)	52	83	166	144	76	7
3	2015/04/24	3.7	3.44	1.6	3.6 (2.1)	4.4 (2.7)	236	82	-137	140	48	-10
4	2015/04/30	3.8	3.51	2.9	2.4 (1.4)	12.5 (7.5)	53	81	166	145	76	9
5	2015/05/23	4.0	3.52	4.0	5.8 (3.5)	14.5 (8.7)	235	66	151	-22	64	27
6	2015/10/13	4.0	3.74	2.7	4.6 (2.8)	10.7 (6.4)	236	64	152	339	65	29
7	2015/12/12	3.8	3.59	2.5	1.7 (1.0)	10.9 (6.5)	57	83	160	149	70	7
8	2016/09/10	4.3	3.66	3.4	2.8 (1.7)	2.3 (1.4)	-14	60	93	160	30	85
9	2017/01/15	3.7	4.07	2.4	3.6 (2.2)	2.1 (1.2)	216	50	104	15	42	74
10	2017/01/15	3.8	3.86	2.8	0.3 (0.2)	0.3 (0.2)	205	26	100	14	64	85
11	2017/01/15	4.3	3.84	2.3	0.9 (0.6)	1.5 (0.9)	216	30	105	19	61	82
12	2017/01/18	4.9	4.11	1.8	3.0 (1.8)	3.5 (2.1)	210	47	116	355	49	65
13	2017/01/27	5.0	4.67	1.8	3.6 (2.1)	4.3 (2.6)	200	42	110	-6	51	73
14	2017/05/04	4.9	4.56	2.4	5.4 (3.2)	16.3 (9.8)	95	76	174	186	84	14
15	2018/12/16	5.7	5.17	3.0	4.6 (2.7)	12.3 (7.4)	79	78	173	170	83	12
16	2019/01/03	5.3	4.82	1.8	5.0 (3.0)	6.4 (3.8)	350	55	47	228	53	134
17	2019/01/15	4.1	4.07	3.0	1.9 (1.2)	3.9 (2.4)	221	42	73	64	50	105
18	2019/01/20	4.0	3.64	0.9	0.5 (0.3)	0.2 (0.1)	14	38	60	230	58	111

Mechanism solutions 1–14 are from Lei *et al.* (2017). Pf^1 and Pf^2 were estimated by assuming $R = 0.023$ (Fig. 8a) and $R = 0.15$ (Fig. 8b), respectively.



▲ Figure 10. Calculated Coulomb stress change (ΔCFS) from the source faults of (strike, dip, rake) = (170, 83, 12) of the M_L 5.7 earthquake to receiver faults of (a) (strike, dip, rake) = (352, 55, 51) and (b) (227, 50, 132), corresponding to the nodal planes of the January 2019 M_L 5.3 earthquake. The friction coefficient is 0.6, and the mean slip and area of the source fault were estimated based on empirical equations (see the Estimation of Overpressure for $M_w > 3.5$ Events for details).

In the case of disposal of wastewater in the Sichuan basin, the largest events may have occurred during the very beginning stages of injections (Lei *et al.*, 2013) as well as later stages (Lei *et al.*, 2008). Wastewater was injected into depleted gas reservoirs of Permian limestone formations, which are associated with anticlines bounded by faults. Because the depleted gas reservoirs demonstrate very good permeability, this may result in quick response of faulting. In the Changning HF sites, because detailed injection data were not open, detailed correlation between HF activities and large earthquakes are not clear. However, as indicated by stacked event rate of apparent foreshocks and aftershocks of $M_L \geq 4.5$ earthquakes (Fig. 5), large events followed growing number of apparent foreshocks, raising the possibility of being able to catch some signs of fault reactivation from earlier seismicity. Seismic b -value and other detailed information of out-of-zone seismicity is a potential indicator. A practically useful hazard model can be made through numerical approaches that involve detailed structures and consider the coupled interactions of fluid flow in faulted porous media and quasidynamic elasticity to investigate the earthquake nucleation, rupture, and arrest processes for cases of induced seismicity.

At the Weixi and Changning shale gas sites, thus far, 23 $M_L \geq 4.0$ events (including 3 $M_L \geq 5.0$ events) had been observed since systematic shale fracking began in 2014. Because shale gas development is on the rise here and at other sites in the Sichuan basin, we assume that these sites will encounter increased likelihood of additional injection-induced seismicity. Potentially seismogenic faults in these sites being poorly known, the risk of $M_L \geq 6$ events induced by shale fracking remains an

open question. The national regulations should be updated with the requirement for operators to take action if some signs of fault reactivation were observed. In addition, HF-induced seismicity observed in the Sichuan basin, together with detailed injection data and 3D geological data, should be fully studied to advance effective risk management techniques to ensure that shale gas fracking can be carried out effectively and safely.

DATA AND RESOURCES

Catalog data used for seismicity analysis and used for hypocenter relocation were downloaded from the China Earthquake Data Center (CEDC, <http://data.earthquake.cn/index.html> [in Chinese], login required). Phase data (P - and S -arrival times) were compiled by CEDC. Waveform data for moment tensor inversion were provided by Data Management Centre of China National Seismic Network at Institute of Geophysics, China Earthquake Administration (Zheng *et al.*, 2010). The Geographic Information Systems (GIS)-based data processing software packs GeoTaos, which were used for statistic analysis, hypocenter relocation, and moment tensor inversion through embedded utilities, stress inversion, overpressure estimation, and Coulomb failure stress calculation, are available for free at <https://staff.aist.go.jp/xinglin-lei/>. The maps and plots were created using the free software GeoTaos_map (developed by Xinglin Lei; <https://staff.aist.go.jp/xinglin-lei/>) and finished with the software CorelDRAW X8. The background topography in the maps is based on the Advanced Land Observation Satellite (ALOS) World 3D-30 m (AW3D30) digital elevation model

data (https://www.eorc.jaxa.jp/ALOS/aw3d30/index_j.htm). All websites were last accessed on February 2019. ↗

ACKNOWLEDGMENTS

The authors thank Editor-in-Chief Zhigang Peng and two anonymous reviewers for their constructive and timely review comments. Wang acknowledges the support of the State Scholarship Fund of China (Number 201804190004).

REFERENCES

- Atkinson, G. M., D. W. Eaton, H. Ghofrani, D. Walker, B. Cheadle, R. Schultz, R. Shcherbakov, K. Tiampo, J. Gu, and R. M. Harrington (2016). Hydraulic fracturing and seismicity in the western Canada sedimentary basin, *Seismol. Res. Lett.* **87**, 631–647, doi: [10.1785/0220150263](https://doi.org/10.1785/0220150263).
- Bao, X., and D. W. Eaton (2016). Fault activation by hydraulic fracturing in western Canada, *Science* **354**, no. 6318, 1406–1409, doi: [10.1126/science.aag2583](https://doi.org/10.1126/science.aag2583).
- Chen, H., X. Meng, F. Niu, Y. Tang, C. Yin, and F. Wu (2018). Microseismic monitoring of stimulating shale gas reservoir in SW China: 2. Spatial clustering controlled by the preexisting faults and fractures, *J. Geophys. Res.* **123**, 1659–1672, doi: [10.1002/2017JB014491](https://doi.org/10.1002/2017JB014491).
- China Earthquake Networks Center (CENC) (2018). Figure collection of 16 December 2018 Xingwen M5.7 earthquake, available at <https://mp.weixin.qq.com/s/4kff7rNwcl-XnjyYN2h4lQ> (last accessed January 2019).
- Cochran, E. S., J. E. Vidale, and S. Tanaka (2004). Earth tides can trigger shallow thrust fault earthquakes, *Science* **306**, 1164–1166, doi: [10.1126/science.1103961](https://doi.org/10.1126/science.1103961).
- Eaton, D. W., and R. Schultz (2018). Increased likelihood of induced seismicity in highly overpressured shale formations, *Geophys. J. Int.* **214**, 751–757, doi: [10.1093/gji/ggy167](https://doi.org/10.1093/gji/ggy167).
- Ellsworth, W. L. (2013). Injection-induced earthquakes, *Science* **341**, 1225942, doi: [10.1126/science.1225942](https://doi.org/10.1126/science.1225942).
- Gephart, J. W., and D. W. Forsyth (1984). An improved method for determining the regional stress tensor using earthquake focal mechanism data: Application to the San Fernando earthquake sequence, *J. Geophys. Res.* **89**, 9305–9320.
- Han, L., Z. Peng, C. W. Johnson, F. F. Pollitz, L. Li, B. Wang, J. Wu, Q. Li, and H. Wei (2017). Shallow microearthquakes near Chongqing, China triggered by the Rayleigh waves of the 2015 M 7.8 Gorkha, Nepal earthquake, *Earth Planet. Sci. Lett.* **479**, 231–240, doi: [10.1016/j.epsl.2017.09.024](https://doi.org/10.1016/j.epsl.2017.09.024).
- Hardebeck, J. L., and A. J. Michael (2006). Damped regional-scale stress inversions: Methodology and examples for southern California and the Coalinga aftershock sequence, *J. Geophys. Res.* **111**, no. B11, doi: [10.1029/2005JB004144](https://doi.org/10.1029/2005JB004144).
- Kim, K.-H., J.-H. Ree, Y. Kim, S. Kim, S. Y. Kang, and W. Seo (2018). Assessing whether the 2017 M_w 5.4 Pohang earthquake in South Korea was an induced event, *Science* **360**, 1007–1009, doi: [10.1126/science.aat6081](https://doi.org/10.1126/science.aat6081).
- Kozłowska, M., M. R. Brudzinski, P. Friberg, R. J. Skoumal, N. D. Baxter, and B. S. Currie (2018). Maturity of nearby faults influences seismic hazard from hydraulic fracturing, *Proc. Natl. Acad. Sci. Unit. States Am.* **115**, E1720–E1729, doi: [10.1073/pnas.1715284115](https://doi.org/10.1073/pnas.1715284115).
- Lei, X., D. Huang, J. Su, G. Jiang, X. Wang, H. Wang, X. Guo, and H. Fu (2017). Fault reactivation and earthquakes with magnitudes of up to M_w 4.7 induced by shale-gas hydraulic fracturing in Sichuan basin, China, *Sci. Rep.* **7**, Article Number 7971, doi: [10.1038/s41598-017-08557-y](https://doi.org/10.1038/s41598-017-08557-y).
- Lei, X., X.-Y. Li, Q. Li, S.-L. Ma, B.-H. Fu, and Y.-X. Cui (2014). Role of immature faults in injection-induced seismicity in oil/gas reservoirs —A case study of the Sichuan basin, China, *Geol. Seismol.* **36**, 625–643, doi: [10.3969/j.issn.0253-4967.2014.03.007](https://doi.org/10.3969/j.issn.0253-4967.2014.03.007) (in Chinese).
- Lei, X., S. Ma, W. Chen, C. Pang, J. Zeng, and B. Jiang (2013). A detailed view of the injection-induced seismicity in a natural gas reservoir in Zigong, southwestern Sichuan basin, China, *J. Geophys. Res.* **118**, 4296–4311, doi: [10.1002/jgrb.50310](https://doi.org/10.1002/jgrb.50310).
- Lei, X., G. Yu, S. Ma, X. Wen, and Q. Wang (2008). Earthquakes induced by water injection at ~3 km depth within the Rongchang gas field, Chongqing, China, *J. Geophys. Res.* **113**, no. B10, doi: [10.1029/2008jb005604](https://doi.org/10.1029/2008jb005604).
- Leonard, M. (2010). Earthquake fault scaling: Self-consistent relating of rupture length, width, average displacement, and moment release, *Bull. Seismol. Soc. Am.* **100**, 1971–1988, doi: [10.1785/0120090189](https://doi.org/10.1785/0120090189).
- Meng, L., A. McGarr, L. Zhou, and Y. Zang (2019). An investigation of seismicity induced by hydraulic fracturing in the Sichuan basin of China based on data from a temporary seismic network, *Bull. Seismol. Soc. Am.* **109**, 348–357, doi: [10.1785/0120180310](https://doi.org/10.1785/0120180310).
- Michael, A. J. (1987). Use of focal mechanisms to determine stress: A control study, *J. Geophys. Res.* **92**, 357, doi: [10.1029/JB092iB01p00357](https://doi.org/10.1029/JB092iB01p00357).
- Norbeck, J. H., and R. N. Horne (2018). Maximum magnitude of injection-induced earthquakes: A criterion to assess the influence of pressure migration along faults, *Tectonophysics* **733**, 108–118, doi: [10.1016/j.tecto.2018.01.028](https://doi.org/10.1016/j.tecto.2018.01.028).
- Okada, Y. (1992). Internal deformation due to shear and tensile faults in a half-space, *Bull. Seismol. Soc. Am.* **82**, 1018–1040.
- Ren, R., B. Qian, J. Zhang, Z. Zhuo, and L. Qio (2015). Practice and understanding of industrial fracturing for shale gas of Longmaxi Formation in Changning region, *Oil Drill. Prod. Technol.* **37**, 96–99, doi: [10.13639/j.odpt.2015.04.025](https://doi.org/10.13639/j.odpt.2015.04.025) (in Chinese with English abstract).
- Rubinstein, J. L., and A. B. Mahani (2015). Myths and facts on wastewater injection, hydraulic fracturing, enhanced oil recovery, and induced seismicity, *Seismol. Res. Lett.* **86**, 1060–1067.
- Schultz, R., G. Atkinson, D. Eaton, Y. Gu, and H. J. S. Kao (2018). Hydraulic fracturing volume is associated with induced earthquake productivity in the Duvernay play, *Science* **359**, 304–308, doi: [10.1126/science.aao0159](https://doi.org/10.1126/science.aao0159).
- Sichuan Earthquake Administration (SEA) (2019). Hazard degree map of the 16 Dec. 2018 M_L 5.7 earthquake, available at http://www.scdzj.gov.cn/dzpd/dzzj/ybxwx57/ljdzyjxy/201812/t20181218_50377.html (last accessed January 2019).
- Sina Corp (2019). Sichuan Xingwen earthquake has injured 17 people and caused direct economy loss over 50 million CNY, available at http://k.sina.com.cn/article_1784473157_6a5ce64502000ybz5.html?from=news&subch=oneWS (last accessed January 2019).
- Skoumal, R. J., M. R. Brudzinski, and B. S. Currie (2015). Earthquakes induced by hydraulic fracturing in Poland Township, Ohio, *Bull. Seismol. Soc. Am.* **105**, 189–197, doi: [10.1785/0120140168](https://doi.org/10.1785/0120140168).
- Skoumal, R. J., R. Ries, M. R. Brudzinski, A. J. Barbour, and B. S. Currie (2018). Earthquakes induced by hydraulic fracturing are pervasive in Oklahoma, *J. Geophys. Res.* **123**, doi: [10.1029/2018JB016790](https://doi.org/10.1029/2018JB016790).
- Terakawa, T., S. A. Miller, and N. Deichmann (2012). High fluid pressure and triggered earthquakes in the enhanced geothermal system in Basel, Switzerland, *J. Geophys. Res.* **117**, doi: [10.1029/2011jb008980](https://doi.org/10.1029/2011jb008980).
- Waldhauser, F., and W. L. Ellsworth (2000). A double-difference earthquake location algorithm: Method and application to the northern Hayward fault, California, *Bull. Seismol. Soc. Am.* **90**, 1353–1368.
- Wang, Y.-m., J.-l. Huang, S.-f. Wang, D.-z. Dong, C.-c. Zhang, and Q.-z. Guan (2016). Dissection of two calibrated areas of the Silurian Longmaxi Formation, Changning and Jiaoshiba, Sichuan basin, *Nat. Gas Geosci.* **27**, 423–432, doi: [10.11764/j.issn.1672-1926.2016.03.0423](https://doi.org/10.11764/j.issn.1672-1926.2016.03.0423) (in Chinese).
- Zadeh, N. S., and S. Talebi (2018). An overview of new developments in shale gas: Induced seismicity aspect, in *Shale Gas—New Aspects and Technologies*, A. Al-Juboury (Editor), IntechOpen, London, United Kingdom, 1–18, doi: [10.5772/intechopen.76542](https://doi.org/10.5772/intechopen.76542).

- Zheng, X.-F., Z.-X. Yao, J.-H. Liang, and J. Zheng (2010). The role played and opportunities provided by IGP DMC of China National Seismic Network in Wenchuan earthquake disaster relief and researches, *Bull. Seismol. Soc. Am.* **100**, 2866–2872.
- Zhu, L., and Y. Ben-Zion (2013). Parametrization of general seismic potency and moment tensors for source inversion of seismic waveform data, *Geophys. J. Int.* **194**, 839–843, doi: [10.1093/gji/ggt137](https://doi.org/10.1093/gji/ggt137).

Xinglin Lei
Zhiwei Wang¹
Geological Survey of Japan
AIST
Higashi 1-1-1, Tsukuba
Ibaraki 305-8567, Japan
xinglin-lei@aist.go.jp
zhiwei-wang@ies.ac.cn

Jinrong Su
Earthquake Monitoring Centre
Sichuan Earthquake Administration
Renming-nan Road 3-29
Chengdu 610041, China
sujr0816@163.com

Published Online 3 April 2019

¹ Also at State Key Laboratory of Earthquake Dynamics, Institute of Geology, China Earthquake Administration, A1#, Hua Yan Li, Chaoyang District, Beijing 100029, China.